J. Fluid Mech. (2006), *vol.* 557, *pp.* 1–27.
doi:10.1017/S0022112006009256 Printed in the United Kingdom

On the formation of sand waves and sand banks

By G. BESIO, P. BLONDEAUX AND G. VITTORI

Department of Environmental Engineering, University of Genova, Via Montallegro 1, 16145 Genova, Italy

(Received 7 October 2004 and in revised form 1 November 2005)

A fully three-dimensional model is proposed for the generation of tidal sand waves and sand banks from small bottom perturbations of a flat seabed subject to tidal currents. The model predicts the conditions leading to the appearance of both tidal sand waves and sand banks and determines their main geometrical characteristics. A finite wavelength of both sand waves and sand banks is found around the critical conditions, thus opening the possibility of performing a weakly nonlinear stability analysis able to predict the equilibrium amplitude of the bottom forms. As shown by previous works on the subject, the sand wave crests turn out to be orthogonal to the direction of the main tidal current. The present results also show that in the Northern Hemisphere sand bank crests are clockwise or counter-clockwise rotated with respect to the main tidal current depending on the counter-clockwise or clockwise rotation of the velocity vector induced by the tide. Only for unidirectional or quasi-unidirectional tidal currents are sand banks always counter-clockwise rotated. The predictions of the model are supported by comparisons with field data. Finally, the mechanisms leading to the appearance of sand waves and sand banks are discussed in the light of the model findings. In particular, it is shown that the growth of sand banks is not only induced by the depth-averaged residual circulation which is present around the bedforms and is parallel to the crests of the bottom forms: a steady drift of the sediment from the troughs towards the crests is also driven by the steady velocity component orthogonal to the crests which is present close to the bottom and can be quantified only by a three-dimensional model. While the former mechanism appears to trigger the formation of counter-clockwise sand banks only, the latter mechanism can give rise to both counter-clockwise and clockwise rotated sand banks.

1. Introduction

The bottom of shallow seas characterized by the presence of tidal currents and large deposits of sand exhibits a variety of regular morphological patterns of different length scales. The largest bedforms are the tidal sand banks recently described in general terms by Dyer & Huntley (1999). Sand banks are periodic morphological patterns with wavelengths ranging a few kilometres and heights which can be even comparable with the water depth. In the Northern Hemisphere, usually the crests of sand banks are slightly counter-clockwise rotated with respect to the principal axis of the tidal ellipse and they hardly move. However, in the North Sea numerous examples do exist of sand banks with crests clockwise rotated with respect to the principal axis of the tidal ellipse, the Sandettie bank and the Zeeland banks being typical examples (Johnson *et al.* 1982; Hommes 2004). At some locations smaller bedforms are present which are called sand waves. The wavelengths of these rhythmic features are of a few hundred metres and they are a few metres high (Belderson, Johnson & Kenyon 1982).

The profile of sand waves is symmetric unless either significant residual currents are present or the tidal wave is asymmetric. In these cases, sand waves migrate, with their crests almost orthogonal to the direction of tide propagation, at a typical rate of about one to some tens of metres per year (Fenster *et al.* 1990) either in the direction of the residual current (Németh, Hulscher & de Vriend 2002) or against it (Besio *et al.* 2004). At some locations, field surveys (Le Bot 2001; Idier 2002; Idier, Astruc & Hulscher 2003; Le Bot & Trenteseaux 2004) show systems of coexisting sand banks and sand waves and provide data on the effects of storms and residual currents on their dynamics.

Previous studies of the processes which lead to the formation of sand banks and sand waves (Huthnance 1982*a*; Hulscher, De Swart & De Vriend 1993; Hulscher 1996) have shown that these regular features arise as free instabilities of the system describing the interaction between the cohesionless sea bottom and the water motions induced by tide propagation.

A possible physical mechanism leading to the formation of tidal sand banks was first suggested by Huthnance (1982*a*, *b*): because of the Coriolis force and bottom frictional effects, the oscillatory tidal flow interacting with bottom forms characterized by crests that are counter-clockwise rotated (in the Northern Hemisphere) with respect to the direction of the main tidal current causes the formation of a clockwise horizontal residual circulation around the crests. Consequently, flow velocities on the upstream side of the crests are slightly higher than those on the downstream side. Since sediment transport increases with increasing velocities, it follows that sediment accumulates at the crests of the bottom waviness. Hulscher *et al.* (1993) tackled the problem using the shallow-water approximation and considering the depth-averaged velocity field. The fastest growing mode determined by Hulscher *et al.* (1993), who in particular considered a unidirectional tide, is characterized by crests almost aligned with the tidal current but slightly counter-clockwise rotated, and the predicted wavelengths are in agreement with the field values. Since the depth-averaged equations cannot describe the vertical recirculating cells which are the driving mechanism of sand wave formation, Hulscher *et al.* (1993) did not look at the conditions leading to sand wave appearance, even though their approach could be extended by an appropriate parametrization of the secondary currents in the vertical plane (see De Swart & Hulscher (1995) where the possible existence of clockwise rotated sand banks is also mentioned).

A more refined model able to describe the formation of both sand waves and sand banks was proposed by Hulscher (1996), who used the shallow-water approximation but did not average along the vertical direction, thus obtaining a description of the vertical recirculating cells which trigger the formation of sand waves. Good predictions of the bedform characteristics were obtained by Hulscher (1996) (see also Hulscher & Van den Brink 2001), even though the model predicts ultra-long wavelengths of the sand banks around the critical conditions and the crests of the sand banks turn out to be always counter-clockwise rotated with respect to the direction of the tidal current. Moreover, the parameters of the model should be tuned as functions of tide and sediment characteristics (Hulscher & Van den Brinks 2001).

Although significant progress has been made both in the prediction of tidal sand banks and sand waves appearance and in the prediction of their characteristics (see De Vriend 1990; Fredsøe & Deigaard 1992; De Swart & Hulscher 1995; Gerkema 2000; Komarova & Hulscher 2000; Komarova & Newell 2000; Besio, Blondeaux & Frisina 2003; Besio *et al.* 2004) much remains to be done. One of the main flaws of the existing models comes from the very simple representation of the flow close to the

bottom: to describe the formation of sand banks, the shallow-water approximation and the depth-averaged velocity have been employed. In the studies of sand wave appearance, turbulent stresses are accounted for by using the Boussinesq hypothesis and by introducing an eddy viscosity which is assumed to be constant over the water depth. In actual flows, turbulent mixing tends to vanish close to a rigid wall, as pointed out by Richards (1980) in his study of ripples and dunes in fluvial environments. In the previous models of tidal sand waves and sand banks, the wall layer is neglected and a partial slip condition at the bottom is introduced for the velocity. It follows that the velocity gradients, which are present close to the bottom and are the main contributions driving the time development of the perturbations (see (3.11*a*)), are greatly underestimated.

In the present contribution, a new model is described which provides both a more reliable description of the processes which lead to the formation of tidal sand banks and sand waves and more accurate predictions of their geometrical characteristics. The model is based on the study of the stability of the flat bottom configuration: small bottom perturbations are considered and a linear analysis of their growth is performed. To describe the hydrodynamics and the morphodynamics of shallow tidal seas, the model proposed by Blondeaux & Vittori (2005*a*, *b*) is used but modified to take into account the local time derivatives of the perturbed velocity field which play an important role in the time development of the sand banks. In fact, the local acceleration terms in the momentum equations, neglected by Blondeaux & Vittori (2005*a*, *b*), have the same order of magnitude as the Coriolis terms which are already known to play a fundamental role in sand bank appearance. In particular, turbulence generated by tidal currents is described by introducing an eddy viscosity which is assumed to depend on the distance from the bottom. Comparisons of the theoretical results with field observations support the model findings.

The procedure used in the rest of the paper is as follows. In the next section we formulate the hydrodynamic problem and we introduce the sediment transport parameterization. In § 3, we determine the basic flow, i.e. the solution describing both the tidal wave propagation over a flat bottom and the sediment transport. We also study the interaction of the tidal current with an arbitrary bottom perturbation. Finally, the results are described in § 4 where a qualitative and quantitative comparison of the theoretical predictions with field observations is also given. A discussion of the physical mechanisms leading to the appearance of sand waves and sand banks is given in § 5. Some conclusions are drawn in § 6 where both ongoing and future research are also outlined.

2. Formulation of the problem

The problem formulation is similar to that described in Blondeaux & Vittori (2005*a*, *b*). We briefly summarize it and refer the interested reader to these papers for more details. A shallow sea of small depth h^* is considered and a Cartesian coordinate system is introduced such that the x^*-axis is along the parallels pointing east, the y^*-axis points north along the meridian line and the z^*-axis is vertical pointing upwards. The seabed is assumed to be made of a cohesionless sediment of uniform size d^* and density ρ_s^* (hereinafter a star denotes dimensional quantities). As pointed out in the Introduction, the aim of the work is to determine the time development of perturbations of the flat bottom configuration forced by tidal currents.

By using the f-plane approximation (see for example LeBlond & Mysak 1978), the problem of flow determination is posed by the continuity and momentum equations

where the Coriolis contributions related to the Earth's rotation (Ω^* is the angular velocity of the Earth's rotation and ϕ_0 is the local latitude) are taken into account because they affect the tidal current. The flow regime is assumed to be turbulent and viscous effects are neglected. An exhaustive analysis of turbulence properties in tidal currents is provided in the review paper of Soulsby (1983). The field measurements of Heathershaw (1979), Bowden & Ferguson (1980), Soulsby (1980, 1981) and Soulsby & Dyer (1981) show that the turbulence can be safely assumed isotropic. Hence, using the Boussinesq hypothesis to model Reynolds stresses, a scalar kinematic eddy viscosity ν_T^* can be introduced.

On defining the following dimensionless variables:

$$(x, y, z) = (x^*, y^*, z^*)/h_0^*, \quad t = t^*\omega^*, \tag{2.1a}$$

$$(u, v, w) = (u^*, v^*, w^*)/U_0^*, \quad p = p^*/\varrho^*\omega^* h_0^* U_0^*, \tag{2.1b}$$

(ρ^* is the sea water density, t^* is time, (u^*, v^*, w^*) are the velocity components along the x^*-, y^*- and z^*-axes, p^* is pressure, h_0^* is the average water depth, ω^* is the angular frequency of the tide, U_0^* is the maximum value of the depth-averaged fluid velocity during the tidal cycle), the flow equations become

$$\frac{\partial u}{\partial x} + \frac{\partial v}{\partial y} + \frac{\partial w}{\partial z} = 0, \tag{2.2}$$

$$\frac{\partial u}{\partial t} + \hat{r}\left[u\frac{\partial u}{\partial x} + v\frac{\partial u}{\partial y} + w\frac{\partial u}{\partial z}\right] = -\frac{\partial p}{\partial x} + \hat{\delta}^2\left\{\frac{\partial}{\partial x}\left[2\nu_T\frac{\partial u}{\partial x}\right] + \frac{\partial}{\partial y}\left[\nu_T\left(\frac{\partial u}{\partial y} + \frac{\partial v}{\partial x}\right)\right] + \frac{\partial}{\partial z}\left[\nu_T\left(\frac{\partial u}{\partial z} + \frac{\partial w}{\partial x}\right)\right]\right\} - 2\Omega[\cos(\phi_0)w - \sin(\phi_0)v], \tag{2.3}$$

$$\frac{\partial v}{\partial t} + \hat{r}\left[u\frac{\partial v}{\partial x} + v\frac{\partial v}{\partial y} + w\frac{\partial v}{\partial z}\right] = -\frac{\partial p}{\partial y} + \hat{\delta}^2\left\{\frac{\partial}{\partial x}\left[\nu_T\left(\frac{\partial u}{\partial y} + \frac{\partial v}{\partial x}\right)\right] + \frac{\partial}{\partial y}\left[2\nu_T\frac{\partial v}{\partial y}\right] + \frac{\partial}{\partial z}\left[\nu_T\left(\frac{\partial v}{\partial z} + \frac{\partial w}{\partial y}\right)\right]\right\} - 2\Omega\sin(\phi_0)u, \tag{2.4}$$

$$\frac{\partial w}{\partial t} + \hat{r}\left[u\frac{\partial w}{\partial x} + v\frac{\partial w}{\partial y} + w\frac{\partial w}{\partial z}\right] = -\frac{g^*}{U_0^*\omega^*} - \frac{\partial p}{\partial z} + \hat{\delta}^2\left\{\frac{\partial}{\partial x}\left[\nu_T\left(\frac{\partial u}{\partial z} + \frac{\partial w}{\partial x}\right)\right] + \frac{\partial}{\partial y}\left[\nu_T\left(\frac{\partial v}{\partial z} + \frac{\partial w}{\partial y}\right)\right] + \frac{\partial}{\partial z}\left[2\nu_T\frac{\partial w}{\partial z}\right]\right\} + 2\Omega\cos(\phi_0)u, \tag{2.5}$$

where the kinematic eddy viscosity ν_T^* is written as the product $\nu_{T0}^*\nu_T$: the constant ν_{T0}^* is dimensional and provides the order of magnitude of the eddy viscosity while $\nu_T = \nu_T(x, y, z, t)$ is a dimensionless function (of order 1) describing the spatial and temporal variations of the turbulence structure. In (2.3)–(2.5), two dimensionless parameters appear which are denoted by $\hat{r}$ and $\hat{\delta}$ respectively:

$$\hat{r} = \frac{U_0^*}{\omega^* h_0^*}, \quad \hat{\delta} = \frac{\sqrt{\nu_{T0}^*/\omega^*}}{h_0^*}. \tag{2.6}$$

The parameter $\hat{r}$ is the ratio between the amplitude of horizontal fluid displacement oscillations and the local depth. Values of $\hat{r}$ are of order 10^2. The parameter $\hat{\delta}$ is the ratio between the thickness of the viscous bottom boundary layer and the local depth. A rough estimate of $\hat{\delta}$ shows that it is of order one. Finally, Ω is the ratio between

the angular velocity of the Earth's rotation and the angular frequency of the tidal wave. For a semidiurnal tide $\Omega \approx 0.5$ while for the diurnal tide component $\Omega \approx 1$.

The hydrodynamic problem is then closed by appropriate boundary conditions. At the free surface, described by $z = \eta(x, y, t)$, the dynamic boundary condition forces the vanishing of the stresses. Moreover, the kinematic boundary condition is forced. Finally, the velocity is forced to vanish at a distance from the seabed equal to a fraction of the dimensionless roughness z_r equal to z_r^*/h_0^*, z_r^* being the size of the bottom roughness.

For later convenience, the dynamic pressure P is introduced

$$p = P - \frac{g^*}{U_0^* \omega^*}(z - \eta). \tag{2.7}$$

The time development of the bottom configuration is provided by the sediment continuity equation, which in dimensionless form is

$$\frac{\partial h}{\partial T} = \frac{\partial q_x}{\partial x} + \frac{\partial q_y}{\partial y} \tag{2.8}$$

where $h = h^*/h_0^*$ is the dimensionless local water depth and (q_x^*, q_y^*), (q_x, q_y) are the dimensional and dimensionless volumetric sediment transport rates per unit width in the x- and y-directions respectively, such that $(q_x, q_y) = (q_x^*, q_y^*)/\sqrt{(\rho_s^*/\rho^* - 1)g^*(d^*)^3}$. The slow time scale

$$T = \frac{td}{(1 - p_{or})\sqrt{\hat{\psi}_d}} \tag{2.9}$$

is introduced. In (2.9) p_{or} is the sediment porosity and d is the dimensionless sediment size which, along with the mobility number $\hat{\psi}_d$ and the Reynolds number R_p characterize the sediment particles

$$d = \frac{d^*}{h_0^*}, \qquad \hat{\psi}_d = \frac{(\omega^* h_0^*)^2}{(\rho_s^*/\rho^* - 1)g^* d^*}, \qquad R_p = \frac{\sqrt{(\rho_s^*/\rho^* - 1)g^* d^{*3}}}{\nu}. \tag{2.10}$$

The sediment Reynolds number R_p is introduced because it appears in the sediment transport predictors.

The problem can be closed once a model for the eddy viscosity ν_T^* is given and relationships for (q_x^*, q_y^*) are provided. The eddy viscosity ν_T^* is assumed to be time-independent and given by

$$\nu_T^* = k \frac{U_0^* h_0^*}{\mathscr{C}} F(\xi). \tag{2.11}$$

In (2.11) k is the von Kármán constant ($k = 0.4$) and the eddy viscosity is assumed to be proportional to the time average of the local friction velocity and to the local depth h_0^*. The average friction velocity is then related to U_0^* by introducing the friction factor $\mathscr{C}$, which only depends on the dimensionless roughness z_r, since the Reynolds number of the flow is assumed to be large. Standard formulae for steady currents can be used to evaluate $\mathscr{C}$. Finally, the function $F(\xi)$ ($\xi = (z^* - \eta^*)/(h^* + \eta^*)$) describes the vertical structure of the eddy viscosity and has been chosen, as suggested by Dean (1974), such that the eddy viscosity grows linearly with the distance from the bed, when a region close to the bottom is considered, and then decreases achieving a finite small value at the free surface. A time-independent eddy viscosity model provides a fair description of the phenomenon because it mainly fails only at flow reversal, when tidal currents are very weak and the transport of any quantity, and in particular of

sediment particles, tends to vanish (Gerkema 2000). Therefore, the morphodynamic consequences of this assumption are negligible. Finally, the eddy viscosity is written in the form $\nu_T^* = \nu_{T0}^* \nu_T(\xi)$ where

$$\nu_{T0}^* = kU_0^* h_0^* \int_{-1}^{0} F(\xi)\,\mathrm{d}\xi/\mathscr{C} \quad \text{and} \quad \nu_T(\xi) = F(\xi)/\int_{-1}^{0} F(\xi)\,\mathrm{d}\xi.$$

These definitions of ν_{T0}^* and ν_T have been chosen in such a way that the depth-averaged value of $\nu_T(\xi)$ is equal to one. Since ν_{T0}^* is proportional to U_0^*, for later convenience, it is useful to introduce the new viscous parameter

$$\hat{\Delta} = \frac{k\displaystyle\int_{-1}^{0} F(\xi)\,\mathrm{d}\xi}{\mathscr{C}} = \frac{\hat{\delta}^2}{\hat{r}} \tag{2.12}$$

which does not depend on the strength of the tidal current.

Sediment transport is usually split into two components. One is due to sediment moving close to the bottom (the 'bed load') and the other is due to sediment which is carried into suspension (the 'suspended load'). Here, the approach proposed by Van Rijn (1991) is used to evaluate the two contributions. In particular, his empirical formula is used to quantify the bed-load components (q_{Bx}, q_{By}) which turn out to depend on the x- and y-components of the dimensionless bed shear stress θ

$$(\theta_x, \theta_y) = \frac{(\tau_x^*, \tau_y^*)}{(\varrho_s^* - \varrho^*) g^* d^*} \tag{2.13}$$

where (τ_x^*, τ_y^*) are the dimensional shear stress components, which can be easily evaluated by means of the constitutive law.

To complete the description of the sediment transport which takes place close to the sea bed, it is necessary to account for the weak effects associated with a slow spatial variation of the bottom topography, which affect the bed-load sediment transport. Assuming that the bottom slope ∇h is small, simple dimensional arguments coupled with linearization lead to the following contribution

$$(q_{Px}, q_{Py}) = -q_B \mathbf{G} \nabla h \tag{2.14}$$

where $\mathbf{G}$ is a dimensionless second-order two-dimensional tensor. Experimental observations of various authors (Talmon, Struiksma & Van Meirlo 1995) provide estimates for the components of $\mathbf{G}$ (Seminara 1998).

To evaluate the suspended sediment transport (q_{Sx}, q_{Sy}), it is necessary to compute the concentration $c = c(x^*, y^*, z^*, t^*)$ by solving a standard convection–diffusion equation:

$$\frac{1}{\hat{r}}\frac{\partial c}{\partial t} + u\frac{\partial c}{\partial x} + v\frac{\partial c}{\partial y} + w\frac{\partial c}{\partial z} - \frac{w_s}{\hat{r}\sqrt{\hat{\psi}_d}}\frac{\partial c}{\partial z} = \hat{\Delta}\left\{\frac{\partial}{\partial x}\left[\nu_T\frac{\partial c}{\partial x}\right] + \frac{\partial}{\partial y}\left[\nu_T\frac{\partial c}{\partial y}\right] + \frac{\partial}{\partial z}\left[\nu_T\frac{\partial c}{\partial z}\right]\right\} \tag{2.15}$$

where w_s is the dimensionless particle fall velocity defined by

$$w_s = w_s^* / \sqrt{\left(\frac{\varrho_s^*}{\varrho^*} - 1\right) g^* d^*}.$$

Suitable boundary conditions are forced at the seabed and at the free surface. The free-surface boundary condition states that the sediment flux in the normal-to-surface

direction $\hat{n}$ must vanish. Then, following Van Rijn (1991), a reference concentration c_{ζ^*} is forced at a distance $\zeta^* = 0.01h^*$ off the seabed.

Once the concentration c is obtained by solving (2.15), the suspended sediment transport q_S can be found as the flux of concentration over the water column:

$$(q_{Sx}, q_{Sy}) = \frac{\hat{r}\sqrt{\hat{\psi}_d}}{d} \int_{-h+\zeta}^{\eta} \left[(u, v)c + \hat{\Delta}\nu_T \left(\frac{\partial c}{\partial x}, \frac{\partial c}{\partial y} \right) \right] \mathrm{d}z. \tag{2.16}$$

However, as suggested by Van Rijn (1991), the suspended load is evaluated neglecting the diffusive part of (2.16) because of the small values usually assumed by the parameter $\hat{\Delta}$ for field conditions, and some numerical experiments suggest that $\hat{\Delta}\nu_T(\partial c/\partial x, \partial c/\partial y)$ provides a negligible contribution to the suspended load.

3. The time development of arbitrary bottom perturbations of small amplitude

Small perturbations of the flat bottom are considered so that the bottom configuration differs from the flat one by a small (strictly infinitesimal) amount proportional to ϵ. Hence, the bottom profile can be thought of as given by the superposition of different spatial components which evolve independently from each other. A normal mode analysis can be performed and the problem can be solved for the generic spatial component

$$h = 1 - \epsilon A(t)\mathrm{e}^{\mathrm{i}(\alpha_x x + \alpha_y y)} + \text{c.c.} + O(\epsilon^2) \tag{3.1}$$

where $\epsilon A(t)$ is the amplitude of the generic component which is periodic in the x- and y-directions with wavenumbers α_x and α_y respectively and $\epsilon \ll 1$. The small value of ϵ allows the solution to be expanded in terms of ϵ:

$$\begin{aligned}[u, v, w, p, \eta, c] = &\left[u_0, v_0, \frac{h_0^*}{L^*} w_0, \frac{L^*}{h_0^*} P_0, \frac{a^*}{h_0^*} e_0, c_0 \right] \\ &+ \epsilon \left[u_1, v_1, w_1, \hat{r} P_1, \left(\frac{a^*}{h_0^*} \right)^2 e_1, c_1 \right] A(t)\mathrm{e}^{\mathrm{i}(\alpha_x x + \alpha_y y)} + \text{c.c.} + O(\epsilon^2). \end{aligned} \tag{3.2}$$

The scaling introduced by (2.1) is appropriate to study the flow induced by the interaction of a tidal wave with bedforms which are characterized by an amplitude and a length of the same order of magnitude as the water depth h_0^*. In this case, the continuity equation suggests that the three velocity components have the same order of magnitude. When a tidal wave propagating over a flat bottom is considered, the most appropriate horizontal length scale turns out to be

$$L^* = \frac{\sqrt{g^* h_0^*}}{\omega^*}. \tag{3.3}$$

Since the ratio h_0^*/L^* is much smaller than one, an analysis of the order of magnitude of the different terms in the continuity equation suggests that the vertical velocity component is of order $h_0^* U_0^*/L^*$. Similarly, the kinematic condition at the free surface suggests that η^* is of order a^*, where $a^* = U_0^* h_0^*/(\omega^* L^*)$ is related to the amplitude of the tidal wave. Also, momentum equation shows that the dynamic pressure P^* is of order $\rho^* U_0^* \omega^* L^*$. Finally, when a bottom waviness of small amplitude ϵh_0^* ($\epsilon \ll 1$) is considered and the flow field is expanded as a power series in ϵ, at the leading order of approximation the balances previously described occur. Then, at the following order of approximation, because of the boundary conditions and continuity equation, the

three velocity components turn out to be of order ϵU_0^*. The above order of magnitude analysis, along with the assumptions

$$\frac{h_0^*}{L^*} \ll 1, \qquad \frac{a^*}{h_0^*} \ll 1, \tag{3.4}$$

justifies (3.2).

At the leading order of approximation, i.e. $O(\epsilon^0)$, the problem is reduced to the determination of both the flow and sediment transport induced by tide propagation over a flat seabed. Here, the solution at the leading order of approximation is assumed to be dominated by the main tide constituent which is indicated by the superscript $^{(1)}$:

$$(u, v, w, P, \eta) = \left(u_0^{(1)}, v_0^{(1)}, \frac{h_0^*}{L^*} w_0^{(1)}, \frac{L^*}{h_0^*} P_0^{(1)}, \frac{a^*}{h_0^*} e_0^{(1)}\right) \mathrm{e}^{-\mathrm{i}t} + \text{c.c.} \tag{3.5}$$

where the functions $u_0^{(1)}$, $v_0^{(1)}$, $w_0^{(1)}$, $P_0^{(1)}$ depend on z and on the slow spatial coordinates

$$X = \frac{h_0^*}{L^*} x, \qquad Y = \frac{h_0^*}{L^*} y. \tag{3.6}$$

By substituting (3.5) and (3.6) into equations (2.2)–(2.5), a set of ordinary differential equations is obtained which can be numerically solved with a shooting procedure to determine the vertical structure of the velocity field for given characteristics of the tidal ellipse (orientation with respect to the x-axis, ratio e_{cc} between the minor and major axes, etc). The details of the solution procedure are described in Blondeaux & Vittori (2005*a*).

Let us only point out that two solutions exist: one describes a clockwise rotating tidal velocity vector, the other describes a counter-clockwise rotating tidal velocity vector. The choice of the former or the latter depends on the propagation of the tidal wave and its interaction with the horizontal boundaries and cannot be made on the basis of this local model. Only field surveys can provide this information as well as the value of e_{cc}. Once the local flow is known, the vertical distribution of sediment concentration can be computed using (2.15) and the appropriate boundary conditions. The fair agreement between the predicted quantities and the data of Knight & Ridgway (1977), who measured the velocity profile in laboratory simulations of oscillatory tidal flows, and the field measurements of Van Rijn, Van Rossum & Ternes (1990) and Chapalain & Thais (2000), who measured both the tidal currents and the sediment concentration, supports the model (see Blondeaux & Vittori 2005*a*).

When (3.2) is substituted into the flow problem formulated in § 2 and terms of order ϵ^2 are neglected, the following set of linear equations for u_1, v_1, w_1, p_1 and e_1 is derived:

$$\mathrm{i}\alpha_x u_1 + \mathrm{i}\alpha_y v_1 + \frac{\partial w_1}{\partial z} = 0, \tag{3.7}$$

$$\begin{aligned} &\frac{1}{\hat{r}A}\frac{\mathrm{d}A}{\mathrm{d}t} u_1 + \frac{1}{\hat{r}}\frac{\partial u_1}{\partial t} + \left[\mathrm{i}\alpha_x u_0 u_1 + \mathrm{i}\alpha_y v_0 u_1 + w_1 \frac{\partial u_0}{\partial z}\right] \\ &\quad = -\mathrm{i}\alpha_x P_1 - \mathrm{i}\alpha_x e_1 + \hat{\Delta}\left[\nu_{T0}\left(\frac{\partial^2 u_1}{\partial z^2} - \alpha_x^2 u_1 - \alpha_y^2 u_1\right) + \frac{\partial \nu_{T0}}{\partial z}\left(\frac{\partial u_1}{\partial z} + \mathrm{i}\alpha_x w_1\right)\right. \\ &\qquad \left. + \nu_{T1}\frac{\partial^2 u_0}{\partial z^2} + \frac{\partial \nu_{T1}}{\partial z}\frac{\partial u_0}{\partial z}\right] - \frac{2\Omega}{\hat{r}}\left[\cos(\phi_0) w_1 - \sin(\phi_0) v_1\right], \end{aligned} \tag{3.8}$$

$$\frac{1}{\hat{r}A}\frac{\mathrm{d}A}{\mathrm{d}t}v_1+\frac{1}{\hat{r}}\frac{\partial v_1}{\partial t}+\left[\mathrm{i}\alpha_x u_0 v_1+\mathrm{i}\alpha_y v_0 v_1+w_1\frac{\partial v_0}{\partial z}\right]$$
$$=-\mathrm{i}\alpha_y P_1-\mathrm{i}\alpha_y e_1+\hat{\Delta}\left[\nu_{T0}\left(\frac{\partial^2 v_1}{\partial z^2}-\alpha_x^2 v_1-\alpha_y^2 v_1\right)+\frac{\partial \nu_{T0}}{\partial z}\left(\frac{\partial v_1}{\partial z}+\mathrm{i}\alpha_y w_1\right)\right.$$
$$\left.+\nu_{T1}\frac{\partial^2 v_0}{\partial z^2}+\frac{\partial \nu_{T1}}{\partial z}\frac{\partial v_0}{\partial z}\right]-\frac{2\Omega}{\hat{r}}\sin(\phi_0)u_1, \tag{3.9}$$

$$\frac{1}{\hat{r}A}\frac{\mathrm{d}A}{\mathrm{d}t}w_1+\frac{1}{\hat{r}}\frac{\partial w_1}{\partial t}+[\mathrm{i}\alpha_x u_0 w_1+\mathrm{i}\alpha_y v_0 w_1]$$
$$=-\frac{\partial P_1}{\partial z}+\hat{\Delta}\left[\nu_{T0}\left(\frac{\partial^2 w_1}{\partial z^2}-\alpha_x^2 w_1-\alpha_y^2 w_1\right)+\mathrm{i}\nu_{T1}\left(\alpha_x\frac{\partial u_0}{\partial z}+\alpha_y\frac{\partial v_0}{\partial z}\right)\right.$$
$$\left.+2\frac{\partial \nu_{T0}}{\partial z}\frac{\partial w_1}{\partial z}\right]+\frac{2\Omega}{\hat{r}}\cos(\phi_0)u_1, \tag{3.10}$$

subject to the following boundary conditions,

$$u_1=-\frac{\partial u_0}{\partial z},\quad v_1=-\frac{\partial v_0}{\partial z},\quad w_1=0\ \text{ at }\ z=-1+\frac{z_r}{29.8}, \tag{3.11a}$$

$$\frac{\partial u_1}{\partial z}=0,\quad \frac{\partial v_1}{\partial z}=0,\quad -P_1+2\hat{\Delta}\nu_{T0}\frac{\partial w_1}{\partial z}=0,\quad w_1=0\ \text{ at }\ z=0, \tag{3.11b}$$

where the eddy viscosity ν_T has been split into a contribution of order one and a contribution of order ϵ which is induced by the bottom perturbation:

$$\nu_T=\nu_{T0}+\epsilon\nu_{T1}A\mathrm{e}^{\mathrm{i}(\alpha_x x+\alpha_y y)}+\text{c.c.}+O(\epsilon^2). \tag{3.12}$$

The functions ν_{T0} and ν_{T1} can be easily computed by expanding the adopted empirical relationships.

The form of (3.7)–(3.11) suggests solving the problem with respect to u_1, v_1, w_1 and the unknown P_1+e_1 (the reader should note that e_1 does not depend on z and the term $\partial e_1/\partial z$ can be added to (3.10)). Then, the value of e_1 can be obtained by means of the boundary condition (3.11b) involving the pressure P_1. This solution procedure shows that the rigid-lid approximation, used in previous works on the subject (Hulscher 1996; Gerkema 2000; Besio *et al.* 2003, 2004) does not introduce any approximation in the evaluation of u_1, v_1, w_1 but does not allow the determination of e_1.

Equation (2.8) shows that $\mathrm{d}A(t)/\mathrm{d}t$ is proportional to $A(t)$ through the ratio between the hydrodynamic and the morphodynamic time scales, which turns out to be proportional to $(1-p_{or})\sqrt{\hat{\psi}_d}/d$ and hence much smaller than one. Therefore, the terms appearing in (3.8)–(3.10), which are proportional to $\mathrm{d}A(t)/\mathrm{d}t$, have been neglected.

In Blondeaux & Vittori (2005*b*), where bottom features smaller than sand banks have been considered, the problem has been solved neglecting the local time derivatives and the Coriolis terms, because of the large values assumed by the parameter $\hat{r}$ for field conditions. However, here, Coriolis effects are important in the process leading to the formation of sand banks and they are of the same order of magnitude as the local time derivatives which, thus, cannot be neglected. Therefore, a solution procedure different from that used by Blondeaux & Vittori (2005*b*) is required because the time t is no longera parameter as in Blondeaux & Vittori (2005*b*). The periodicity of the

basic flow suggests writing the unknown functions u_1, v_1, w_1, p_1 as Fourier series in time

$$(u_1, v_1, w_1, p_1) = \sum_{n=-\infty}^{\infty} \left(u_1^{(n)}, v_1^{(n)}, w_1^{(n)}, p_1^{(n)}\right) \mathrm{e}^{\mathrm{i}nt}. \tag{3.13}$$

By substituting (3.13) into (3.7)–(3.10), a linear system of coupled ordinary differential equations for the unknown functions $(u_1^{(n)}, v_1^{(n)}, w_1^{(n)}, p_1^{(n)})$ is derived. The solution is numerically obtained with a shooting procedure similar to that described in Vittori (1989). Starting from the free surface ($z = 0$), a set of linearly independent numerical solutions is determined by forcing the boundary conditions (3.11*b*) and by fixing linearly independent values for the free variables at the free surface. The numerical procedure makes use of a coordinate stretching to increase the number of grid points close to the bottom where the velocity gradients are larger and employs a standard Runge–Kutta method of the second order. The final solution is then determined as a linear combination of the above solutions which satisfies the boundary conditions at the sea bottom. Numerical experiments, with successive grid refinements, suggest the number of grid points which are required to ensure the reliability and the accuracy of the results.

Once the velocity perturbations are computed, the perturbed concentration can be evaluated by solving the differential problem

$$\frac{1}{\hat{r}A}\frac{\mathrm{d}A}{\mathrm{d}t}c_1 + \frac{1}{\hat{r}}\frac{\partial c_1}{\partial t} + \left[\mathrm{i}\alpha_x u_0 c_1 + \mathrm{i}\alpha_y v_0 c_1 + w_1 \frac{\partial c_0}{\partial_z}\right] - \frac{w_s}{\hat{r}\sqrt{\hat{\psi}_d}}\frac{\partial c_1}{\partial z}$$
$$= \hat{\Delta}\left[\nu_{T0}\left(\frac{\partial^2 c_1}{\partial z^2} - \alpha_x^2 c_1 - \alpha_y^2 c_1\right) + \frac{\nu_{T0}}{\partial z}\left(\frac{\partial c_1}{\partial z}\right) + \nu_{T1}\frac{\partial^2 c_0}{\partial z^2} + \frac{\partial \nu_{T1}}{\partial z}\frac{\partial c_0}{\partial z}\right], \tag{3.14}$$

$$c_1 + \frac{\partial c_0}{\partial z} - c_{\zeta_1} = 0 \ \text{ at } \ z = -1 + 0.01, \quad \frac{w_s}{\hat{r}\sqrt{\hat{\psi}_d}}c_1 + \hat{\Delta}\left[\nu_{T0}\frac{\partial c_1}{\partial z} + \nu_{T1}\frac{\partial c_0}{\partial z}\right] = 0 \ \text{ at } \ z = 0, \tag{3.15}$$

where c_{ζ_1} is a term of $O(\epsilon)$ for the reference concentration at the bottom. The solution of (3.14) subject to (3.15) is determined by writing

$$c_1 = \sum_{n=-\infty}^{\infty} c_1^{(n)} \mathrm{e}^{\mathrm{i}nt} \tag{3.16}$$

and using a procedure similar to that previously described.

Then perturbations of the bottom shear stresses and of the sediment transport rates

$$(q_{Bx}, q_{By}, q_{Sx}, q_{Sy}, \ldots) = (q_{Bx0}, q_{By0}, q_{Sx0}, q_{Sy0}, \ldots)$$
$$+ \epsilon A(t)(q_{Bx1}, q_{By1}, q_{Sx1}, q_{Sy1}, \ldots)\mathrm{e}^{\mathrm{i}(\alpha_x x + \alpha_y y)} + \text{c.c.} + O(\epsilon^2) \tag{3.17}$$

can be readily evaluated. Since the algebra, though straightforward, is lengthy and tedious, we omit the details.

The equation which provides the time development of the amplitude of the bottom perturbation follows from the sediment continuity equation:

$$\frac{\mathrm{d}A(T)}{\mathrm{d}T} = \gamma(t)A(T) \tag{3.18}$$

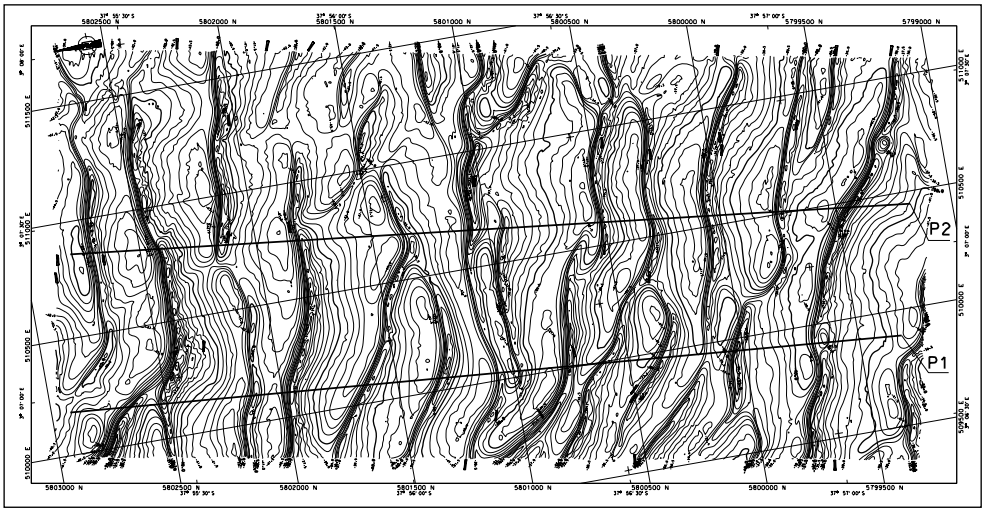

FIGURE 1. Bottom topography measured at 52° 21′ N and 3° 9′ E showing the presence of sand waves. The grid size is 500 m. Courtesy of SNAM PROGETTI.

where γ is a periodic, complex function of t which depends on the parameters of the problem and can be decomposed as

$$\gamma(t) = \{\mathrm{i}(\alpha_x q_{Bx1} + \alpha_y q_{By1}) + \mathrm{i}(\alpha_x q_{Sx1} + \alpha_y q_{Sy1}) + \mathrm{i}(\alpha_x q_{Px1} + \alpha_y q_{Py1})\}. \tag{3.19}$$

The solution of (3.18)

$$A(T) = A_0 \exp\left[\int_0^T \gamma(t')\,\mathrm{d}t'\right] \tag{3.20}$$

shows that the growth or the decay of the bottom perturbation is controlled by the real part $\overline{\gamma}_R$ of the time average $\overline{\gamma}$ of γ, while the imaginary part $\overline{\gamma}_I$ is related to the migration speed of the perturbations. Because of the symmetry of the forcing flow, no migration of the bottom forms is expected and indeed $\overline{\gamma}_I$ vanishes. The remaining periodic parts of γ ($\gamma - \overline{\gamma}$) describe the oscillations of the bottom forms around their average configuration. These oscillations turn out to be quite small since the tide period is much smaller than the morphodynamic time scale. Different contributions to the amplification rate γ of the bottom perturbation can be identified according to the mechanisms of sediment transport. The largest contributions (the first and third terms on the right-hand side of (3.19)) are related to the bed load and to the slope effects, the latter being always real and negative and tending to stabilize any bottom waviness. The value of γ is also affected by the suspended load even though it becomes important only when the mobility number is large.

4. Discussion of the results

Because of the large number of parameters controlling the phenomenon, we start by comparing the theoretical results with some field observations. Subsequently, we investigate the role of the main parameters (tide characteristics, sediment parameters, etc.) involved in the formation of sand wave and sand bank.

4.1. *Prediction of the sand wave characteristics*

The bathymetric data of the first site which we analyse are those measured at 52° 21′ N and 3° 9′ E by SNAM PROGETTI S.p.A. and shown in figure 1. The average water

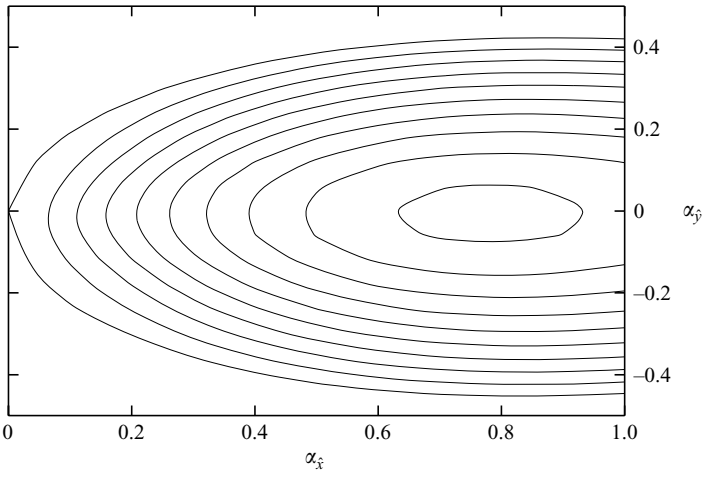

FIGURE 2. Growth rate $\overline{\gamma}_R$ plotted versus $\alpha_{\hat{x}}$ and $\alpha_{\hat{y}}$ for $\hat{r} = 72$, $e_{cc} = 0.17$, $\hat{\Delta} = 0.00325$, $R_p = 15.90$, $\hat{\psi}_d = 0.0083$, $d = 6.25 \times 10^{-6}$. Only positive isolines are displayed with $\Delta\overline{\gamma}_R = 0.003$. The maximum value of $\overline{\gamma}_R$ is located at $(\alpha_{\hat{x}}, \alpha_{\hat{y}}) \simeq (0.79, 0)$.

depth is about 40 m and a wavy bed (sand waves) characterized by a wavelength of about 285 ± 85 m and heights ranging between 3.5 m and 5.5 m is present. The harmonic analysis of the tidal current measured at two nearby locations shows that the tide is mainly semi-diurnal with M2 as the dominant constituent. The amplitude of the velocity oscillations induced by the M2 constituent during the measuring period (15 October 1988–31 March 1989) is about 0.41 m s^{-1} and the direction of the velocity is almost orthogonal to the crests of the sand waves. The ratio between the minor and major axes of the tidal ellipse, denoted in the following e_{cc}, is about 0.17 and the tidal velocity vector is counter-clockwise rotating. The sediment turns out to have $d_{50}^* = 0.25$ mm. Unfortunately, no information was available about the bottom roughness which is supposed to be due to seabed ripples 0.3 m long and 5 cm high.

To show the capability of the model to predict the appearance of sand waves, the real part $\overline{\gamma}_R$ of the time average of the function γ is obtained as function of $\alpha_{\hat{x}}$ and $\alpha_{\hat{y}}$ for values of the parameters chosen in order to reproduce the local climate and sediment characteristics. The $\hat{x}$- and $\hat{y}$-axes are horizontal such that $\hat{x}$ is aligned with the major axis of the tidal ellipse.

The results obtained (figure 2) show that the bedforms which tend to appear are characterized by crests almost orthogonal to the major axis of the tidal ellipse, as observed in the field, since the maximum value of $\overline{\gamma}_R$ is reached for practically vanishing values of $\alpha_{\hat{y}}$. The perturbation component characterized by the maximum amplification rate, i.e. the component which will dominate the bottom configuration for long times, is characterized by $(\alpha_{\hat{x}}, \alpha_{\hat{y}}) \simeq (0.79, 0)$. These wavenumbers correspond to a dimensional wavelength of about 320 m, a value similar to the observed wavelengths that fall between 200 m and 370 m.

The second field site (51° 35′ N and 3° 2′ E) has an average water depth (20 m) smaller than the previous case and the observed sand waves are characterized by a wavelength equal to 210 ± 45 m (see figure 3). The amplitude of the velocity oscillations induced by the dominant M2 constituent is about 0.43 m s^{-1} and the tidal velocity vector is counter-clockwise rotating. The value of e_{cc} is equal to 0.42. The sediment is coarser than the previous case and characterized by $d_{50}^* = 0.60$ mm. Figure 4 shows

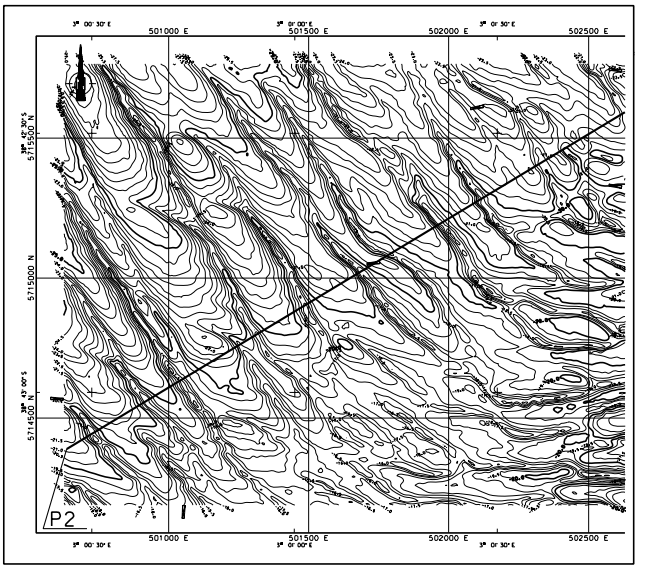

FIGURE 3. Bottom topography measured at 51° 35′ N and 3° 2′ showing the presence of sand waves. The grid size is 500 m. Courtesy of SNAMPROGETTI.

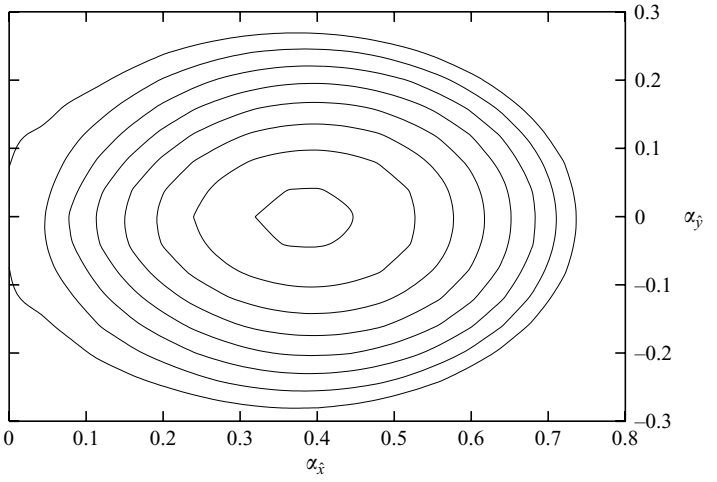

FIGURE 4. Growth rate $\overline{\gamma}_R$ plotted versus $\alpha_{\hat{x}}$ and $\alpha_{\hat{y}}$ for $\hat{r} = 148$, $e_{cc} = 0.42$, $\hat{\Delta} = 0.00347$, $R_p = 59$, $\hat{\psi}_d = 0.00087$, $d = 3.0 \times 10^{-5}$. Only positive isolines are displayed with $\Delta\overline{\gamma}_R = 0.0005$. The maximum value of $\overline{\gamma}_R$ is located at $(\alpha_{\hat{x}}, \alpha_{\hat{y}}) \simeq= (0.39, 0)$.

that the most unstable bottom perturbation turns out to have the crests orthogonal to the main tidal axis and a wavelength of about 320 m, a value which is not far from the observed sand wave spacing. At this stage, it is important to emphasize that the present model has no parameter which can be tuned to make the theoretical results fit the field data.

In order to efficiently investigate the effect of the main parameters of the model on the sand wave formation, a one-dimensional investigation has been made by fixing $\alpha_{\hat{y}} = 0$. Figure 5 shows $\overline{\gamma}_R$ versus $\alpha_{\hat{x}}$ for the same values of the parameters as in figure 4 but for different values of $\hat{r}$. For a semidiurnal tide at a particular site, where

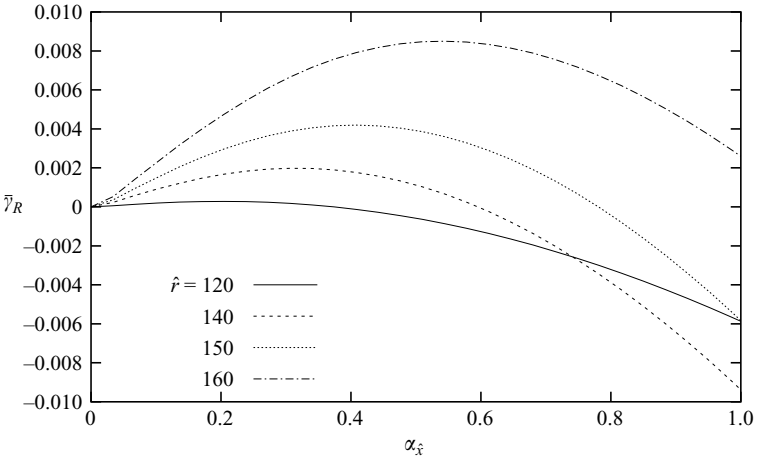

FIGURE 5. Growth rate $\overline{\gamma}_R$ plotted versus $\alpha_{\hat{x}}$, fixing $\alpha_{\hat{y}} = 0$ for $e_{cc} = 0.42$, $\hat{\Delta} = 0.00347$, $R_p = 59$, $\hat{\psi}_d = 0.00087$, $d = 3.0 \times 10^{-5}$ and different values of $\hat{r}$.

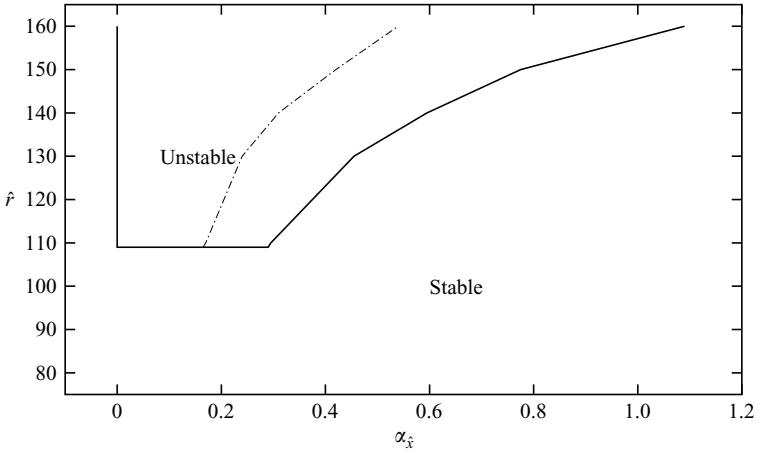

FIGURE 6. Marginal stability conditions plotted in the plane $(\alpha_{\hat{x}}, \hat{r})$ for the same values of the parameters as figure 5. Dash-dotted line represents the location of the relative maximum of the amplification rate $\overline{\gamma}_R(\alpha_{\hat{x}})$.

the water depth and sediment characteristics are fixed, different values of $\hat{r}$ imply different amplitudes of the depth-averaged velocity oscillations induced by the tide and hence different values of the bed shear stress. For constant values of ω^* and h_0^*, the variations of $\hat{r}$ are linked to variations of U_0^* which in turn induce variations of (τ_x^*, τ_y^*) and then of (θ_x, θ_y). When the strength of the tide is increased, the values of $\overline{\gamma}_R$ grow showing that the flat bottom configuration is more unstable. Moreover, the value of $\alpha_{\hat{x}}$, which gives rise to the maximum value of $\overline{\gamma}_R$, increases thus showing that stronger tidal currents generate shorter sand waves. On the other hand, when $\hat{r}$ is decreased, smaller values of $\overline{\gamma}_R$ are found till, for $\hat{r}$ smaller than a critical value $\hat{r}_{CW}$, which in the site under consideration is about 110, no sediment motion takes place. Therefore, the model suggests that, in the North Sea site considered, the flat bottom configuration is stable only when the Shields parameter is smaller than its critical value and no sediment is moved during the tidal cycle. In figure 6 the marginal stability conditions

are shown in the plane $(\alpha_{\hat{x}}, \hat{r})$ for the same values of the parameters as those of figure 5. The critical value $\hat{r}_{CW}$ of $\hat{r}$, below which sand waves do not appear, can be easily estimated from the figure, which also shows that a finite range of $\alpha_{\hat{x}}$ becomes unstable once $\hat{r}$ becomes larger than its critical value. The maximum amplification rate for a fixed value of $\hat{r}$ takes place for the value of $\alpha_{\hat{x}}$ which is indicated by a dash-dotted line in figure 6 and tends to a finite value $\alpha_{\hat{x}_C}$ ($\alpha_{\hat{x}_C} = 0.17$) as $\hat{r}$ tends to $\hat{r}_{CW}$.

An extensive investigation of the effects of sediment size has shown that, for a coarse sand and a moderate tidal current (see for example the data of figure 2), the real part of $\overline{\gamma}_S$ vanishes and the growth/decay of the bottom perturbations is controlled by a balance between the destabilizing effect due to the bed load and the stabilizing one due to the bottom slope. When fine sand and a strong tidal current are considered, the suspended load provides a relevant contribution to the time development of the bottom. In particular, in the range of the paramenters analysed here, the real part of $\overline{\gamma}_S$ turns out to be always negative and therefore the sediment carried into suspension provides a stabilizing contribution to $\overline{\gamma}_R$.

The stability analysis described in §§ 3 and 4 is linear and, hence, unable to provide any information on the equilibrium amplitude attained by the growing perturbation for long times. Indeed, once the amplitude $A(t)$ of the bottom waviness grows and reaches large values, nonlinear effects become strong and the analysis fails. However, the present model can be extended to cover the weakly nonlinear regime by considering a neighbourhood of the critical conditions and the perturbation characterized by the largest amplification rate, which the present results show to have a finite wavelength.

4.2. *Prediction of the sand bank characteristics*

The present linear analysis provides further information on the configuration of the sea bottom forced by a tidal wave: since the model is based on the full three-dimensional momentum equations, it can describe the processes leading to both sand waves and sand banks.

To ascertain the capability of the model to predict the appearance of sand banks and their characteristics, the amplification rate $\overline{\gamma}_R$ of bottom perturbations has been computed for values of the parameters chosen to reproduce the coastal region of the Norfolk banks and in particular of the Well Bank, Broken Bank and Swarte Bank system described by Collins *et al.* (1995) (see figure 7). The average water depth is about 30 m and the sea bed consists of well-sorted fine-graded sand (the grain size is assumed to be equal to 0.15 mm). On the basis of the current measurements described in Collins *et al.* (1995), the system is assumed to be forced by a semidiurnal tide constituent with amplitude of the velocity oscillations equal to $0.7\,\mathrm{m\,s^{-1}}$. Moreover, the tidal ellipse has been assumed to be characterized by a value of e_{cc} equal to 0.2 and the major axis to form an angle equal to 140° with the north direction. The seabed roughness is fixed equal to 5 cm (seabed ripples are assumed to be present). Finally, numerical models of tide propagation and the data described in Collins *et al.* (1995) suggest that the tide velocity is clockwise rotating. Figure 8, where the amplification rate $\overline{\gamma}_R$ of bottom perturbations is plotted as function of $\alpha_{\hat{x}}$ and $\alpha_{\hat{y}}$, shows that the most unstable perturbation is characterized by $(\alpha_{\hat{x}}, \alpha_{\hat{y}}) \approx (0.012, -0.031)$, i.e. it is a two-dimensional waviness with crests almost aligned with the direction of the mean tidal current but forming an angle of about 20° and being counter-clockwise rotated. Moreover, the predicted wavelength turns out to be about 5.5 km. These predicted geometrical characteristics are in good agreement with field data, as the observed sand

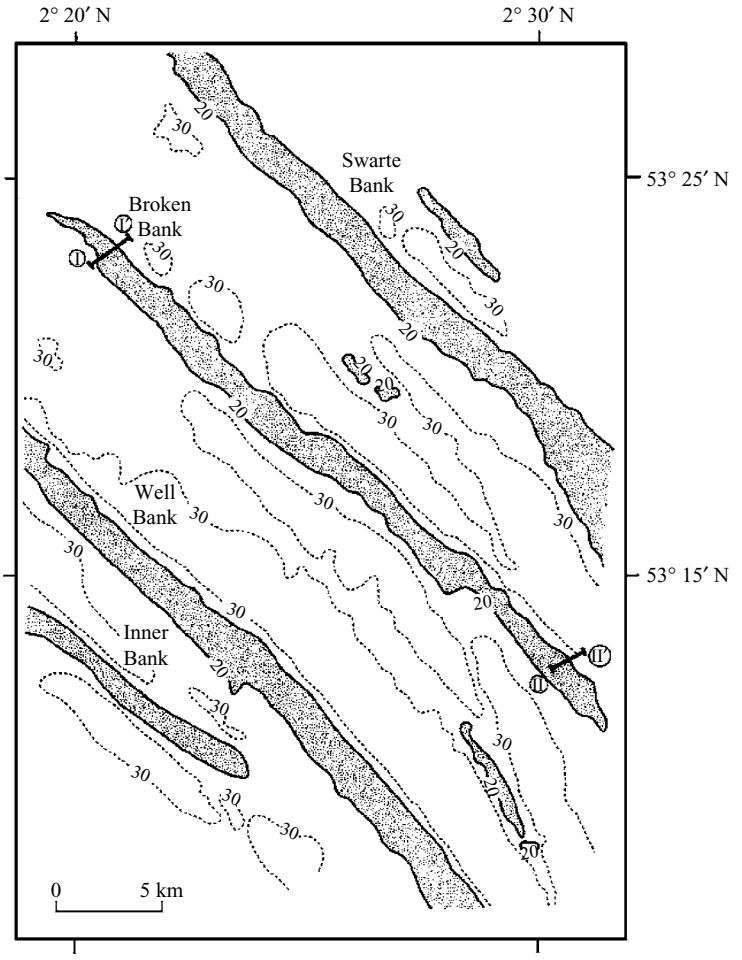

FIGURE 7. Bathymetry (in metres) of the Well Bank, Broken Bank and Swarte Bank system. Adapted from Collins *et al.* (1995).

banks are slightly counter-clockwise rotated with respect to the main tidal current and are characterized by a wavelength ranging between 4 and 10 km.

Next, a coastal region, where tidal sand banks are characterized by crests clockwise rotated with respect to the direction of the major axis of the tidal ellipse, has been considered. The region is located in front of the coast of the Dutch provinces Zeeland and Zuid-Holland, seaward of the −20 m depth contour, where many tidal ridges can be detected: Bollen Van Goeree (1), Steenbanken (2), Middelbank (3), Schouwenbank (4), Buitenbanken (5), Schaar (6), Rasbank (7) and Thorntonbank (8) (see figure 9 adapted from Hommes 2004). The average spacing of the banks is between 2 and 3 km. The whole area, except for a nearshore region of 5–14 km, is also covered with sand waves with wavelengths between 100 and 800 m (Hommes 2004). The local sand has a diameter ranging between moderate coarse sand (210–300 μm) and very coarse sand (300–420 μm). To evaluate the tidal current the measurement carried out at (51° 30′*N*, 3° 2′*E*) by SNAM PROGETTI S.p.A., between 15 October 1988 and 31 March 1989, have been used: the tide is dominated by the semidiurnal constituent, with the maximum amplitude of the depth-averaged velocity oscillations equal to

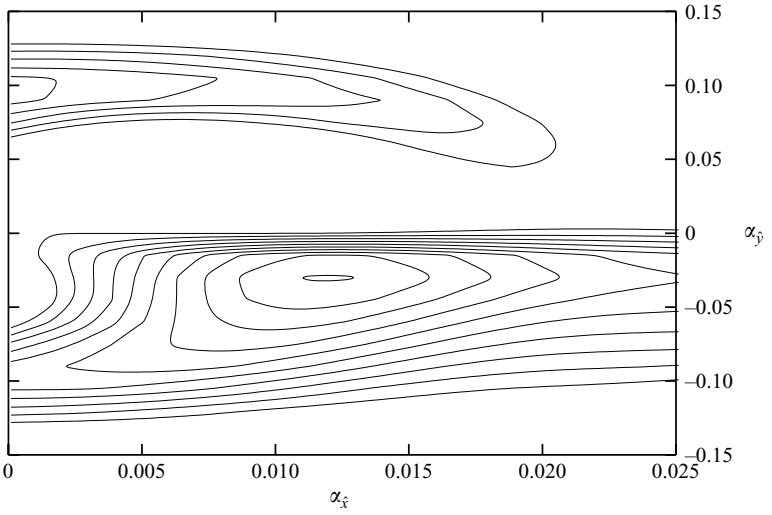

FIGURE 8. Growth rate $\overline{\gamma}_R$ plotted versus $\alpha_{\hat{x}}$ and $\alpha_{\hat{y}}$ for $\hat{r} = 160$, $e_{cc} = 0.20$, $\hat{\Delta} = 0.00288$, $R_p = 7.39$, $\hat{\psi}_d = 0.00779$, $d = 5.0 \times 10^{-5}$ and a clockwise rotating tidal velocity vector. Only positive isolines are displayed with $\Delta\overline{\gamma}_R = 0.002$. The maximum value of $\overline{\gamma}_R$ is located at $(\alpha_{\hat{x}}, \alpha_{\hat{y}}) \simeq (0.012, -0.031)$.

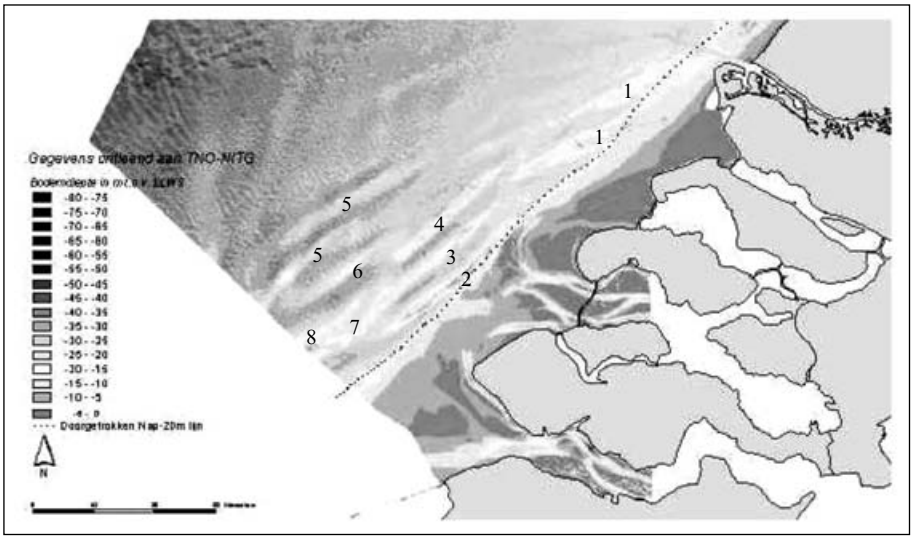

FIGURE 9. Bathymetry of Zeeland ridges. Adapted from Hommes (2004).

$0.43\,\mathrm{m\,s^{-1}}$. The value of e_{cc} is 0.4 and the tidal vector is counter-clockwise rotating. Figure 10 shows the amplification rate $\overline{\gamma}_R$ of bottom perturbations plotted versus $(\alpha_{\hat{x}}, \alpha_{\hat{y}})$. A relative maximum is present for $(\alpha_{\hat{x}}, \alpha_{\hat{y}}) \approx (0.013, 0.030)$, i.e. for ridges characterised by a wavelength of about 3.8 km and by crests clockwise rotated with respect to the major axis of the tidal ellipse (23°). Also in this case, the geometrical characteristics of the tidal sand banks predicted by the theory are in fair agreement with those observed in the field which, in particular, have crests clockwise rotated with respect to the main tidal current direction (Hommes 2004).

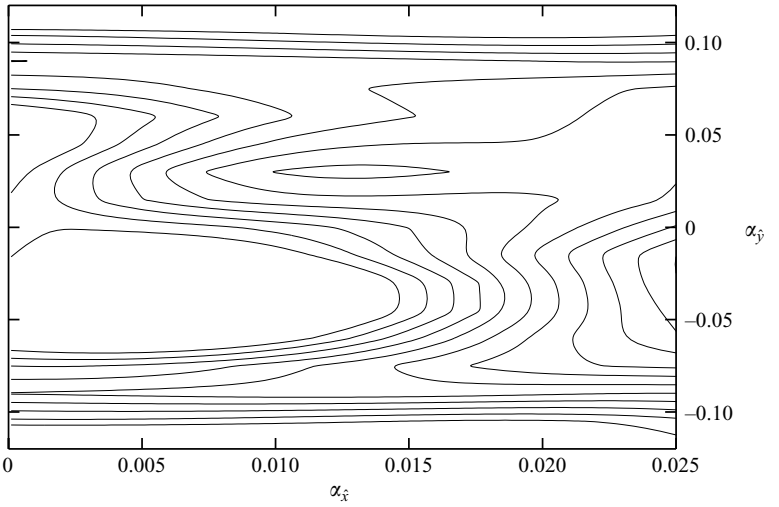

FIGURE 10. Growth rate $\overline{\gamma}_R$ plotted versus $\alpha_{\hat{x}}$ and $\alpha_{\hat{y}}$ for $\hat{r} = 119$, $e_{cc} = 0.4$, $\hat{\Delta} = 0.00321$, $R_p = 15.90$, $\hat{\psi}_d = 0.0032$, $d = 1 \times 10^{-5}$ and a counter-clockwise rotating tidal velocity vector. Only positive isolines are displayed with $\Delta\overline{\gamma}_R = 0.00008$. The maximum value of $\overline{\gamma}_R$ is located at $(\alpha_{\hat{x}}, \alpha_{\hat{y}}) \simeq = (0.013, 0.030)$.

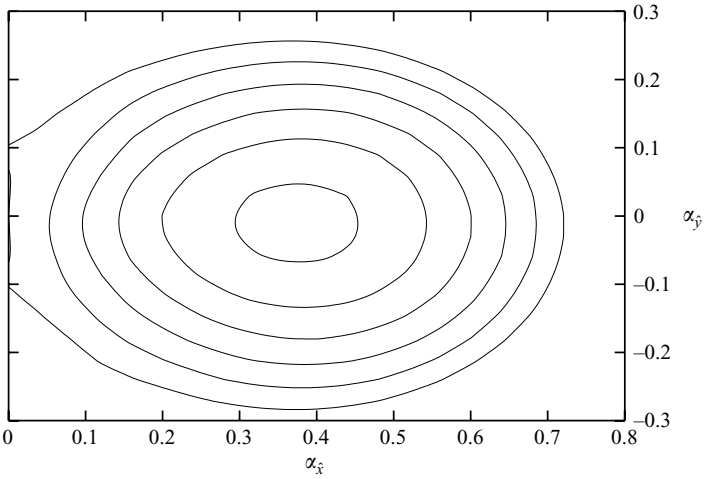

FIGURE 11. Growth rate $\overline{\gamma}_R$ plotted versus $\alpha_{\hat{x}}$ and $\alpha_{\hat{y}}$ for $\hat{r} = 119$, $e_{cc} = 0.4$, $\hat{\Delta} = 0.00321$, $R_p = 15.90$, $\hat{\psi}_d = 0.0032$, $d = 1 \times 10^{-5}$. Only positive isolines are displayed with $\Delta\overline{\gamma}_R = 0.002$. The maximum value of $\overline{\gamma}_R$ is located at $(\alpha_{\hat{x}}, \alpha_{\hat{y}}) \approx (0.38, 0)$.

Figure 11 shows the amplification rate $\overline{\gamma}_R$ plotted for the same values of the parameters as in figure 10, but considering a different range of the wavenumbers of the bottom perturbations. From the results plotted in figure 11, it appears that a second relative maximum of the amplification rate is present for $(\alpha_{\hat{x}}, \alpha_{\hat{y}}) \approx (0.38, 0.0)$. Hence, the theory predicts the simultaneous appearance of sand waves (bedforms with crests orthogonal to the major axis of the tidal ellipse) characterized by a wavelength of about 330 m, a value falling within the range of the observed wavelengths.

The results described so far seem to indicate that a clockwise rotating tidal ellipse gives rise to sand banks with crests counter-clockwise rotated with respect to the main tidal current, while a counter-clockwise rotating tidal ellipse gives rise to clockwise

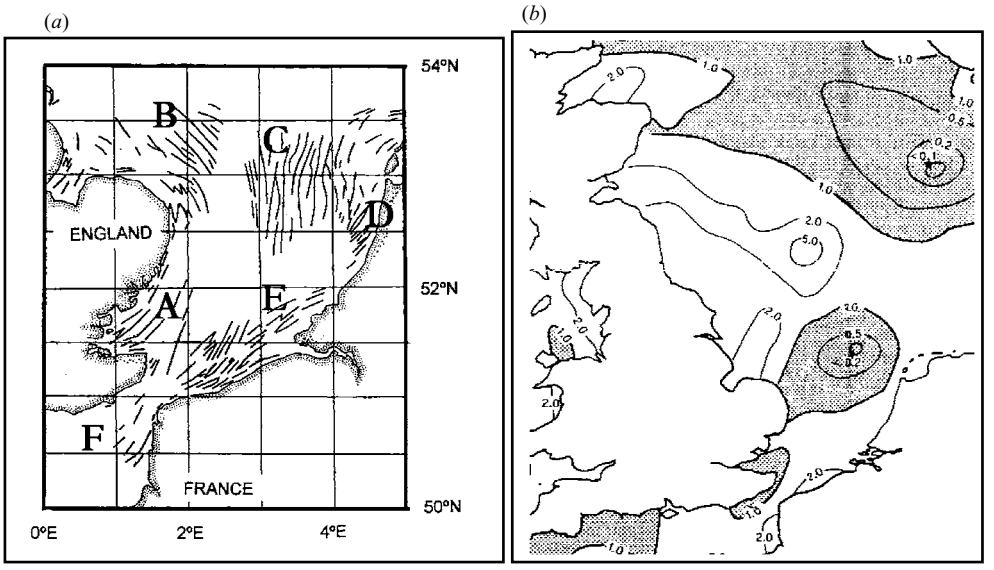

FIGURE 12. (*a*) Patches of tidal sand banks present in the North Sea. Adapted from Dyer & Huntley (1999). (*b*) Ratio of the counter-clockwise to the clockwise rotary component of depth-averaged velocity of the mean spring tide in the seas around the British Isles. Shaded regions have a net clockwise rotation of the current vector. Results from the numerical model of Flather (1976). Adapted from Soulsby (1983).

rotated bedforms. Further runs not reported here support this general finding, even though the large number of parameters involved in the problem has not allowed a fully exhaustive investigation of the phenomenon. Figure 12(*a*), adapted from Dyer & Huntley (1999), shows the main sand banks observed in the North Sea between England and the continental part of Europe. These sand banks have been grouped into six groups: group A is offshore of the Thames estuary, group B is offshore of the Norfolk coast, groups C and D are located offshore of the coast of The Netherlands, group D being closer to the coast, the fifth and sixth groups (groups E and F) are between England and France. Sand banks of groups A, B and C have crests counter-clockwise rotated with respect to the main tidal current. Analogously, with a few exceptions, sand banks of groups D, E and F have their crests clockwise rotated with respect to the main tidal current. In figure 12(*b*), the North Sea is split into regions where the tide has a net clockwise rotation of the current vector (shaded regions) and a net counter-clockwise rotation of the current vector (white regions). As predicted by the model, a high correlation between clockwise rotating tidal velocity vectors and counter-clockwise rotated sand banks and vice versa clearly appears. However, it is worth pointing out that for small values of e_{cc}, i.e. for almost unidirectional tidal currents, no difference is present in the morphological patterns generated by a clockwise rotating tidal velocity and a counter-clockwise rotating tidal velocity. Indeed, the present results show that in the limit of vanishing values of e_{cc}, the growth of counter-clockwise rotated sand banks is always triggered. In the literature, other hypotheses have been made to explain the clockwise/counter-clockwise rotation of the sand banks with respect to the direction of the tidal current. In particular, it has been suggested that the average slope of the seabed could induce a rotation of the sand bank crests just as a transverse variation of the water depth can induce the

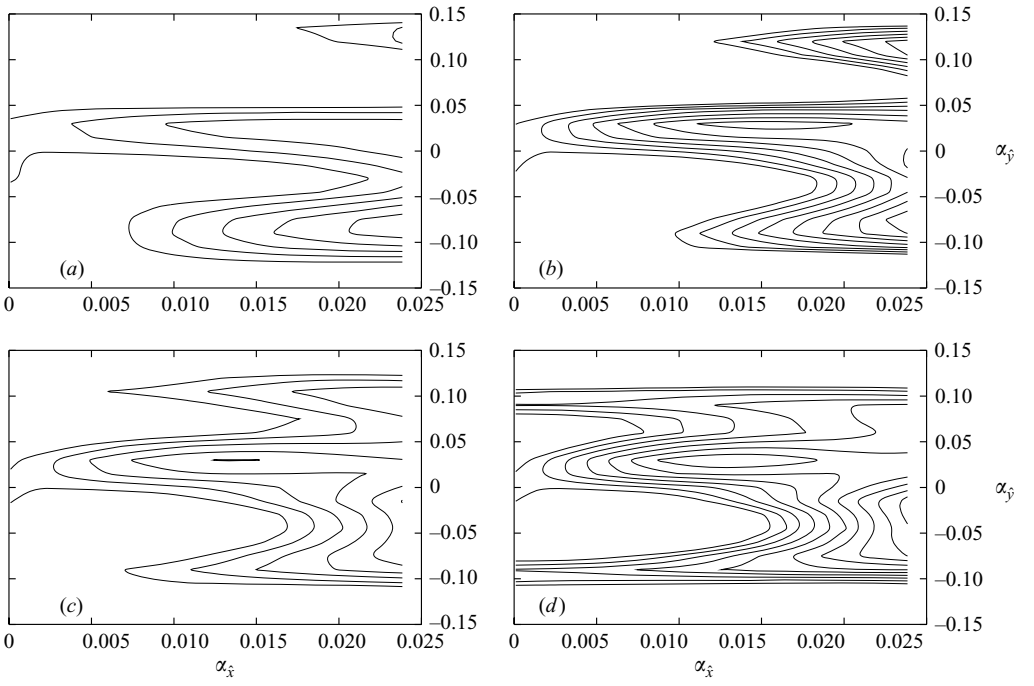

FIGURE 13. Growth rate $\overline{\gamma}_R$ plotted versus $\alpha_{\hat{x}}$ and $\alpha_{\hat{y}}$ for $e_{cc} = 0.4$, $\hat{\Delta} = 0.00321$, $R_p = 15.90$, $\hat{\psi}_d = 0.0032$, $d = 1 \times 10^{-5}$, and (*a*) $\hat{r} = 80$, (*b*) $\hat{r} = 90$, (*c*) $\hat{r} = 100$ and (*d*) $\hat{r} = 110$. Only positive isolines are displayed with $\Delta\overline{\gamma}_R = 0.00001$ for $\hat{r} = 80$ and $\Delta\overline{\gamma}_R = 0.000015$ for $\hat{r} = 90$ and $\Delta\overline{\gamma}_R = 0.00005$ for $\hat{r} = 100, 110$.

growth of oblique dunes in alluvial channels (Engelund 1974). However, no accurate comparison between model predictions and field data has been made.

If the parameter $\hat{r}$ is varied, it can be seen that, on decreasing $\hat{r}$, a critical value $\hat{r}_{CB}$ is encountered below which sand banks no longer form, even though the growth of sand waves is still triggered (see figure 13). In the site described by figure 13, only when $\hat{r}$ is smaller than a second critical value $\hat{r}_{CW}$ ($\hat{r}_{CW} < \hat{r}_{CB}$), does the flat bottom configuration turn out to be stable and neither sand wave nor sand bank are triggered. Moreover, when $\hat{r}$ becomes larger than $\hat{r}_{CB}$, the most unstable large-scale perturbation has a finite wavelength. Hence, the present model allows a weakly nonlinear stability analysis of sand banks growth to be developed.

5. Comments on the physical mechanisms leading to the formation of sand waves and sand banks

As already pointed out in the Introduction, the mechanism which gives rise to the formation of sand waves is due to the appearance of steady and superharmonic velocity components generated by the interaction of the forcing oscillatory tidal current with the bottom waviness. When the hydrodynamic and morphodynamic parameters (in particular the wavelength of the bottom waviness) are such that the sediment is steadily dragged by these velocity components from the troughs towards the crests of the bottom perturbation, the latter grow and gives rise to sand waves. The appearance of a steady streaming and velocity oscillations in all overtones of the basic frequency by an oscillatory flow interacting with curved boundaries is a

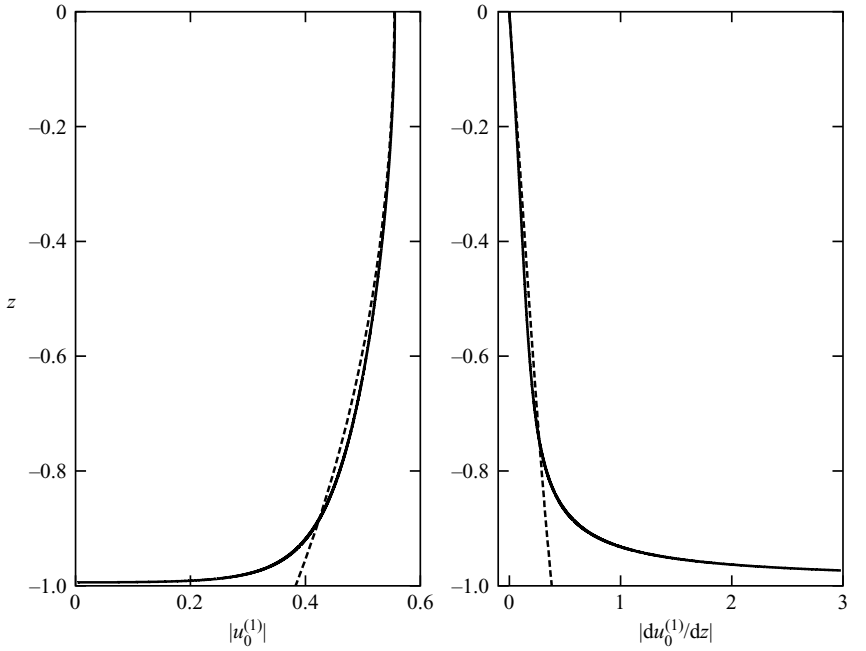

FIGURE 14. Moduli of $u_0^{(1)}$ and $\mathrm{d}u_0^{(1)}/\mathrm{d}z$ versus z for a unidirectional tide and $\hat{r} = 72$, $\hat{\Delta} = 0.00325$, $\Omega = 0.5$, $\phi = 52^\circ 21'$ N. (Present model: continuous line, Besio *et al.*'s (2003) model: broken line). The value of $\mathrm{d}u_0^{(1)}/\mathrm{d}z$ at the bottom predicted by the present model is of order 10^3 and the figure has been cut for the sake of clearness.

well-known phenomenon (see e.g. Schlichting 1932; Stuart 1966). Also, in coastal morphodynamics the mechanism is well known since Sleath (1976) pointed out that the appearance of ripples under sea waves is related to the steady streaming induced by the interaction of the oscillatory flow in the viscous boundary layer with bottom perturbations. However, even though the mechanism was qualitatively well known, accurate quantitative predictions of the steady recirculating cells induced by tidal currents over a wavy bottom were not available. Hulscher (1996) was the first to tackle the problem and solved it using the shallow-water approximation. However, Gerkema (2000) pointed out that the approach used by Hulscher (1996) implicitly assumes that the ratio K between the amplitude of the fluid displacement oscillations in the horizontal direction and the wavelength of the bottom forms is much smaller than one. In the field, K turns out to be much larger than one and Gerkema (2000) improved Hulscher's (1996) solution by determining the steady streaming by means of a perturbation approach which considers large values of K. However, to obtain the solution in closed form, Gerkema (2000) used a constant-eddy-viscosity model and considered large values of the stress parameter s appearing in the partial slip condition at the bottom. Such large values of s make the velocity profile of the basic tidal current more similar to that found in the laminar regime rather than to the velocity profile observed in actual turbulent flows. Besio *et al.* (2003) solved the problem for any finite values of K and s but they still used a constant-eddy-viscosity model. In actual flows, turbulent mixing tends to vanish close to the bottom and hence in Besio *et al.*'s (2003) analysis, the wall layer is neglected and the flow perturbations assume unrealistic small values at the bottom. In figure 14, the moduli

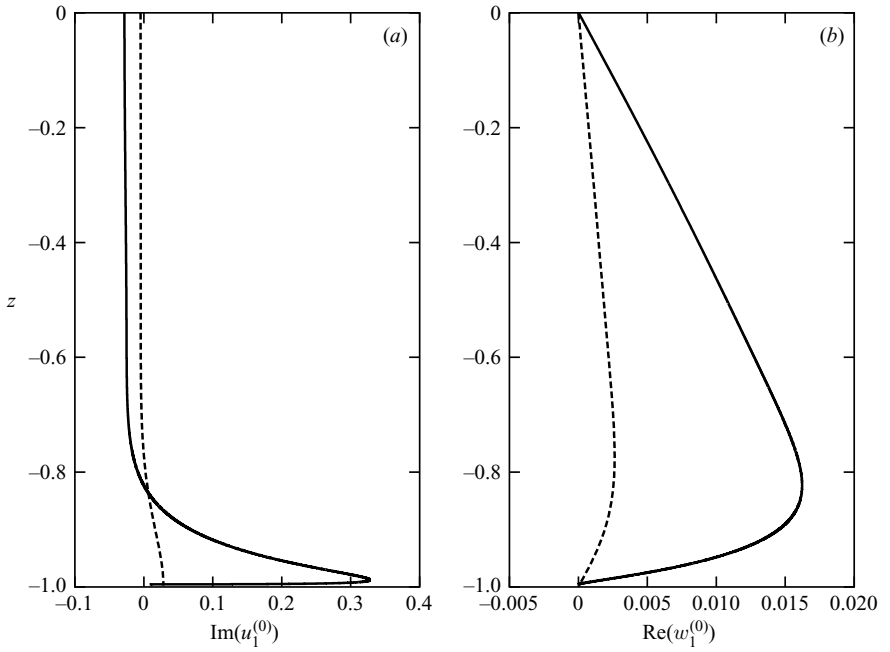

FIGURE 15. Steady streaming generated by an oscillatory unidirectional tidal current over a two-dimensional wavy wall for $\hat{r} = 72$, $\hat{\Delta} = 0.00325$, $\Omega = 0.5$, $\phi = 52^\circ\,21'$ N and $\alpha_{\hat{x}} = 0.8$. (Present model: continuous line, Besio *et al.*'s (2003) model: broken line). (*a*) Imaginary part of $u_1^{(0)}$, (*b*) real part of $w_1^{(0)}$. (The real part of $u_1^{(0)}$ and the imaginary part of $w_1^{(0)}$ vanish both in the present model and in Besio *et al.*'s (2003) model.)

of $u_0^{(1)}$ and $\mathrm{d}u_0^{(1)}/\mathrm{d}z$ obtained by means of the present model and those provided by the constant-eddy-viscosity model of Besio *et al.* (2003) are plotted versus z for a unidirectional tide aligned with the x-axis. The velocity profiles fairly agree but the vertical velocity gradients close to the bottom differ by orders of magnitude. The two models provide similar shear stresses but the present model has much larger values of $\mathrm{d}u_0^{(1)}/\mathrm{d}z$ at the bottom because of the vanishing values of the eddy viscosity at the wall. Since $\mathrm{d}u_0^{(1)}/\mathrm{d}z$ is the forcing term of the problem at $O(\epsilon)$ (see (3.11)), large differences are expected between the results of the constant-eddy-viscosity model and those of the present model. Indeed, figure 15, which shows a comparison between the steady streaming predicted on the basis of the present model and that computed using Besio *et al.*'s (2003) model for the same hydrodynamic parameters, provides evidence of such differences. In fact, the imaginary part of $u_1^{(0)}$ predicted by the present model rapidly increases in a thin layer close to the bottom and then steadily decreases to reach an almost constant value, thus displaying a two-layer structure which is not predicted by Besio *et al.* (2003). Therefore, the present model and the solution procedure described in § 3 greatly improve the description of the flow field and in turn the predictions of sand wave characteristics compared to those obtained by means of previous models which appear to be more postdictive, in the sense of Saffman (1989), than predictive. In fact, previous approaches often require a long tuning procedure of the model parameters to give results in agreement with field surveys.

Since the wavelength of the sand banks is much larger than the local water depth, the process which leads to the formation of sand banks is often analysed by

considering the depth-averaged velocity field

$$(U, V) = \frac{1}{h}\int_{-h}^{a\eta}(u, v)\,\mathrm{d}z \tag{5.1}$$

and by using a simple sediment transport predictor such that the sediment transport rate (q_x, q_y) is proportional to the b-power of the depth-averaged velocity field (Hulscher *et al.* 1993):

$$(q_x, q_y) \sim [\sqrt{U^2 + V^2}]^b \left[\frac{(U, V)}{\sqrt{U^2 + V^2}}\right]. \tag{5.2}$$

The first term on the right of (5.2) quantifies the amount of sand moved by the tidal current and the second one provides the direction.

Because of the presence of a bottom waviness of small amplitude ϵ, it is possible to write

$$(U, V) = (U_0, V_0) + \epsilon\left[(U_1, V_1)A(t)\mathrm{e}^{\mathrm{i}(\alpha_x x + \alpha_y y)} + \text{c.c.}\right] + O(\epsilon^2). \tag{5.3}$$

Then, using a Cartesian coordinate system $(\tilde{x}, \tilde{y})$, with the $\tilde{x}$-axis parallel to the crests of the bottom forms, and introducing the velocity components $(\tilde{U}, \tilde{V})$, it can be easily verified (Besio *et al.* 2005) that the depth-averaged continuity equation at order ϵ leads to

$$\tilde{V}_1 = \tilde{V}_0, \tag{5.4}$$

i.e. no steady velocity component at $O(\epsilon)$ is generated in the direction orthogonal to the crests of the bottom forms but only an oscillatory velocity component characterized by the same frequency as the basic tidal current. Then, the momentum equation shows the existence of a velocity component parallel to the bedform crests $(\tilde{U}_1)$ with a steady part and all the overtones of the basic tidal frequency which are generated by a cascade process.

In the literature (Huthnance 1982*a*, *b*; Hulscher *et al.* 1993), it is assumed that sand banks start to appear because of the presence of the residual depth-averaged circulation around the bedform crests (steady component of $\tilde{U}_1$). In the Northern Hemisphere, an anticyclonic residual circulation is indeed generated around the crest. Hence, when the orientation of the bank is slightly cyclonic with respect to the flow direction, the total flow velocity is slightly increased upstream of the crest whereas it is decreased downstream of the crest, during both the flood and ebb phases of the tide. Since the sediment flux is proportional to some power of the velocity, there is a net convergence of the sediment at the crest which tends to cause the growth of the bank. When the orientation of the bank is anticyclonic, the total flow velocity is slightly decreased upstream of the crest whereas it is increased downstream of the crest and, hence, the bottom waviness is damped. Therefore, this physical mechanism can only explain the appearance of sand banks characterized by crests which are counter-clockwise oriented with respect to the direction of the tidal current, and in the literature it is usually stated that, in the Northern Hemisphere, sand banks should be counter-clockwise rotated. However, field surveys and the present model show the existence of clockwise oriented sand banks, too. Thus, other effects must play an important role in the growth of sand banks. A relevant effect, already pointed out by De Swart & Hulscher (1995), is the deviation, induced by the Coriolis terms, of the direction of the velocity close to the bottom from the direction of the depth-averaged velocity. This phenomenon,which cannot be described by means of a depth-averaged

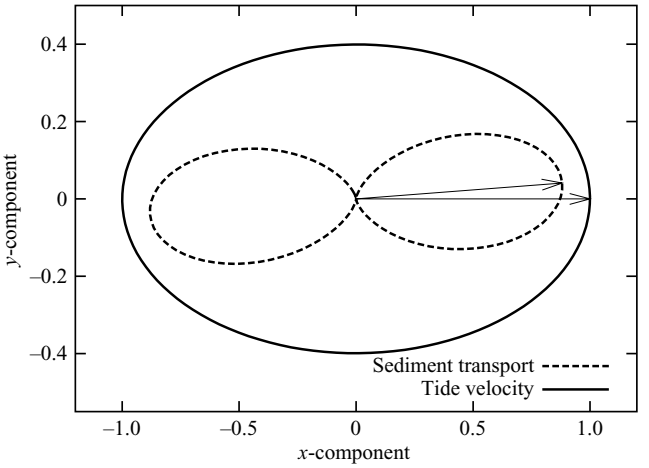

FIGURE 16. Time development of the x- and y-components of the dimensionless sediment transport rate (dashed line) and dimensionless depth-averaged velocity (continous line) calculated for values of the parameters representing the Zeeland Ridges. The value of the sediment transport rate is multiplied by 10 for the sake of clarity.

approach, changes the sediment transport rate (q_{x0}, q_{y0}) from the vector (U_0, V_0) as clearly appears in figure 16, which shows the depth-averaged velocity ellipse and the sediment transport rate predicted by the present three-dimensional model for the Zeeland Bank case. Because of the different direction of the sediment transport rate with respect to the depth-averaged velocity, a net sediment transport component orthogonal to the bedform crests exists which is not accounted for in the models of Huthnance (1982*a*, *b*) and Hulscher *et al.* (1993) and can induce the growth of clockwise rotated sand banks.

Even though a depth-averaged approach cannot predict the deviation of the sediment transport rate from the direction of the depth-averaged velocity, a heuristic correction can be added to the sediment transport predictor to account for this three-dimensional effect (see also De Swart & Hulscher 1995):

$$(q_x, q_y) \sim [\sqrt{U^2 + V^2}]^b \frac{(U\cos\varphi - V\sin\varphi,\, V\cos\varphi + U\sin\varphi)}{\sqrt{U^2 + V^2}}. \tag{5.5}$$

The relevance of the angle φ in the process which leads to the appearance of sand banks clearly appears if the growth rate γ of the bottom perturbations is predicted by means of the shallow-water approximation and the use of (5.5), modified to account for the effects associated to the bottom slope, as made by Besio, Blondeaux & Vittori (2005). Indeed, in Besio *et al.* (2005) it is shown that the sand banks are predicted to be always counter-clockwise rotated if φ is set equal to zero. However, if appropriate values of φ are chosen, the sand banks turn out to be counter-clockwise rotated for a unidirectional tidal current (no difference can exist between clockwise and counter-clowise rotating velocity vectors when e_{cc} is equal to zero), but they are clockwise/counter-clockwise rotated for counter-clockwise/clockwise rotating velocity vectors once e_{cc} assumes significant values. The main advantage of the present three-dimensional model consists in the correct estimate of φ which does not require any heuristic assumption.

6. Conclusions

In this paper, we reinforce the idea that a model, based on the study of the time development of small bottom perturbations of a shallow tidal sea, can explain the formation of both sand waves and sand banks and can also give reliable quantitative predictions of their geometrical characteristics, as shown by the comparison of the theoretical results with field data from different sites obtained without tuning any parameters. The model predictions appear to be good when compared with the results provided by other morphodynamic stability analyses which are used to predict the characteristics of coastal bedforms (Blondeaux 2001). Quite often, comparisons between theoretical predictions and laboratory and/or field data are made just by considering the order of magnitude of the results or looking at their qualitative behaviour (e.g. Trowbridge 1995; Vittori, De Swart & Blondeaux 1999; Coco, Huntley & O'Hare 2000; Komarova & Hulscher 2000; Komarova & Newell 2000; Gerkema 2000; Calvete *et al.* 2001, etc.). In particular, the model predicts a finite wavelength for both sand waves and sand banks at the critical conditions, thus enabling a weakly nonlinear analysis of the phenomenon. This possible analysis should also allow the investigation of the interaction between different modes and the prediction of the final complex configuration of the sea bottom when different types of bedforms coexist. Moreover, the sand banks predicted by the model turn out to be clockwise/counter-clockwise rotated with respect to the main tidal current for counter-clockwise/clockwise rotating tidal velocity vector as shown by field surveys. Only for a unidirectional tidal current are sand banks always counter-clockwise rotated.

The model formulated in the paper provides a simplified description of the actual phenomenon, but it takes into account all the main processes affecting the growth of bottom forms (e.g. oscillating tidal currents, bed load, suspended load, longitudinal and transverse bottom slope effects on sediment transport). Of course some aspects could be improved. For example, a better turbulence model capable of describing the time variation of the turbulence structure during the tidal cycle could be introduced and the effects of wind waves could be taken into account. However, we feel that only minor changes of currently obtainable quantitative predictions would be induced at the expenses of a major effort in the analysis.

This research has been supported by the EU under the contracts n. EVK3-2000-22014 (HUMOR) and n. EVK3-2001-00053 (SANDPIT). At the initial stage funding was also provided by SNAMPROGETTI S.p.A. (contract number 3000000248) and by the University of Genova. The authors wish to thank Prof. Maurizio Brocchini, Dr. L. Iovenitti and Dr. M. Drago for their collaboration during the early stages of the work.

REFERENCES

Belderson, R. H, Johnson, M. A. & Kenyon, N. H. 1982 Bedforms. In *Offshore Tidal Sands.* (ed. A. H. Stride). Chapman & Hall.

Besio, G. 2004 Modelling of tidally generated large scale bedforms. PhD Thesis, University of Genova.

Besio, G., Blondeaux, P., Brocchini, M. & Vittori, G. 2004 On the modelling of sand wave migration. *J. Geophys. Res.* **109**, C04018, doi:10.1029/2002JC001622.

Besio, G., Blondeaux, P. & Frisina, P. 2003 A note on tidally generated sand waves. *J. Fluid Mech.* **485**, 171–190.

Besio, G., Blondeaux, P. & Vittori, G. 2005 Sand bank formation: comparison between 2D and 3D models. *4th IAHR Symposium on River, Coastal and Estuarine Morphodynamics, Urbana, Illinois, October 4–7* (ed. G. Parker & M. Garcia).

Blondeaux, P. 2001 Mechanics of coastal forms. *Annu. Rev. Fluid Mech.* **33**, 339–370.

Blondeaux, P. & Vittori, G. 2005*a* Flow and sediment transport induced by tide propagation. Part 1: the flat bottom case. *J. Geophys. Res.* **110**, C07020.

Blondeaux, P. & Vittori, G. 2005*b* Flow and sediment transport induced by tide propagation. Part 2: the wavy bottom case. *J. Geophys. Res.* **110**, C08003.

Bowden, K. F. & Ferguson, S. R. 1980 Variation with height of the turbulence in a tidally-induced bottom boundary layer. In *Marine Turbulence*. (ed. J. C. J. Nihoul), pp. 259–286. Elsevier.

Calvete, D., Falques, A., De Swart, H. E. & Walgreen, M. 2001 Modelling the formation of shoreface-connected sand ridges on storm-dominated inner shelves. *J. Fluid Mech.* **441**, 169–193.

Chapalain, G. & Thais, L. 2000 Tide, turbulence and suspended sediment modelling in the eastern English Channel. *Coastal Engng* **41**, 295–316.

Coco, G., Huntley, D. A. & O'Hare, T. J. 2000 Investigation of a self-organized model for beach cusp formation and development. *J. Geophys. Res.* **105**, 21991–22002.

Collins, M. B., Shimwell, S. J., Gao, S., Powell, H., Hewistom, C. & Taylor, J. A. 1995 Water and sediment movement in the vicinity of linear sandbanks: the Norfolk Banks, southern North Sea. *Mar. Geol.* **123**, 125–142.

Dean, R. B. 1974 *AERO Rep.* 74-11, Imperial College, London.

De Swart, H. E. & Hulscher, S. J. M. H. 1995 Dynamics of large-scale bed forms in coastal seas. In *Nonlinear Dynamics and Pattern Formation in the Natural Environment* (ed. A. Doelman & A. Van Harten). Longman.

De Vriend, H. J. 1990 Morphological processes in shallow tidal seas. In *Residual Currents and Long-term Transport* (ed. R. T. Cheng). Springer.

Dyer, K. R. & Huntley, D. A. 1999 The origin, classification and modelling of sand banks and ridges. *Cont. Shelf Res.* **19**, 1285–1330.

Engelund, F. 1974 The development of oblique dunes. *Rep.* 32, pp. 37–40, Inst. Hydrodyn. and Hydraulic Engng., Tech. Univ. Denmark.

Fenster, M. S., Fitzgerald, D. M., Bohlen, W. F., Lewis, R. S. & Baldwin, C. T. 1990 Stability of giant sand waves in eastern Long Island Sound, U.S.A. *Mar. Geol.* **91**, 207–225.

Flather, R. A. 1976 A tidal model of the north-west European continental shelf. *Mem. Soc. R. des Sci. Liege* **6**, X, 144–164.

Fredsøe, J. & Deigaard, R. 1992 *Mechanics of Coastal Sediment Transport*. World Scientific.

Gerkema, T. 2000 A linear stability analysis of tidally generated sand waves *J. Fluid Mech.* **417**, 303–322.

Heathershaw, A. D. 1979 The turbulence structure of the bottom boundary layer in a tidal current. *Geophys. J. R. Astron. Soc.* **58**, 395–430.

Hommes, S. 2004 Large-scale sand extraction on sand ridges offshore of the Netherlands. *Tech. Rep.* University of Twente.

Hulscher, S. J. M. H. 1996 Tidal-induced large-scale regular bed form patterns in a three-dimensional shallow water model. *J. Geophys. Res.* **101**, 20727–20744.

Hulscher, S. J. M. H., De Swart, H. E. & De Vriend, H. J. 1993 The generation of offshore tidal sand banks and sand waves. *Cont. Shelf Res.* **13**, 1183–1204.

Hulscher, S. J. M. H. & Van den Brink, G. M. 2001 Comparison between predicted and observed sand waves and sand banks in the North Sea. *J. Geophys. Res.* **106**, 9327–9338.

Huthnance, J. M. 1982*a* On one mechanism forming linear sand banks. *Est. Coastal Shelf Sci.* **14**, 79–99.

Huthnance, J. M. 1982*b* On the formation of sand banks of finite extent. *Est. Coastal Shelf Sci.* **15**, 277–299.

Idier, D. 2002 Dynamics of continental shelf sandbanks and sandwaves: in situ measurements and numerical modeling. PhD Thesis, National Polytechnical Institute, Toulouse Est., France.

Idier, D., Astruc, D. & Hulscher, S. J. M. H. 2003 Short-term dynamics of a Dover Strait tidal sand wave covered by megaripples. *3rd IAHR Symposium on River, Coastal and Estuarine Morphodynamics Barcelona, Spain. September 1–5* (ed. A. Sánchez-Arcilla & A. Bateman).

Johnson, M. A., Kenyon, N. H., Belderson, R. H. & Stride, A. H. 1982 Sand transport. In *Offshore Tidal Sands.* (ed. A. H. Stride). Chapman & Hall.

KNIGHT, D. W. & RIDGWAY, M. A. 1977 Velocity distribution in unsteady open channel flow with different boundary roughness. *Proc. 17th IAHR Congress, Baden-Baden, F.R. Germany,* vol. 2 (ed. Plate & Friedrich) pp. 437–444.

KOMAROVA, N. L. & HULSCHER, S. J. M. H. 2000 Linear instability mechanism for sand wave formation. *J. Fluid Mech.* **413**, 219–246.

KOMAROVA, N. L. & NEWELL, A. C. 2000 Nonlinear dynamics of sand banks and sand waves. *J. Fluid Mech.* **415**, 285–312.

LEBLOND, P. H. & MYSAK, L. A. 1978 *Waves in the Ocean.* Elsevier.

LE BOT, S. 2001 Morphodynamics of submarine dunes under the influence of tides and storms. PhD Thesis, University of Lille 1.

LE BOT, S. & TRENTESEAUX, A. 2001 Types of internal structure and external morphology of submerine dunes under the influence of tidal and wind-driven processes (Dover Strait, Northern France). *Mar. Geol.* **211**, 143–168.

NÉMETH, A. A., HULSCHER, S. J. M. H. & DE VRIEND, H. J. 2002 Modelling sand wave migration in shallow shelf seas. *Cont. Shelf Res.* **22**, 2795–2806.

RICHARDS, K. J. 1980 The formation of ripples and dunes on an erodible bed. *J. Fluid Mech.* **99**, 597–618.

SAFFMAN, P. G. 1980 Coherent structures in turbulent flows. In *The role of Coherent Structures in Modelling Turbulence and Mixing* (ed. J. Jimenez). Springer.

SCHLICHTING, H. 1932 Berechnung ebener periodscher Grenzschichtströmungen. *Phys. Z.* **33**, 327–335.

SEMINARA, G. 1998 Stability and morphodynamics. *Meccanica.* **33**, 59–99.

SLEATH, J. F. A. 1976 On rolling grain ripples. *J. Hydraul. Res.* **14**, 69–81.

SOULSBY, R. L. 1980 Selecting record length and digitization rate for near-bed turbulence measurements. *J. Phys. Oceanogr.* **10**, 208–219.

SOULSBY, R. L. 1981 Measurements of the Reynolds stress components close to a marine sand bank. *Mar. Geol.* **42**, 35–47.

SOULSBY, R. L. 1983 The bottom boundary layer of shelf seas. In *Physical Oceanography of Coastal and Shelf Sea.* (ed. B. John), pp. 189–266. Elsevier.

SOULSBY, R. L. & DYER, K. R. 1981 The form of the near bed velocity profile in a tidally accelerating flow. *J. Geophys. Res.* **86**, 8067–8074.

STRIDE, A. H. 1982 *Offshore Tidal Sands.* Chapman & Hall.

STUART, J. T. 1966 Double boundary layers in oscillatory viscous flow. *J. Fluid Mech.* **24**, 673–687.

TALMON, A. M., STRUIKSMA, N. & VAN MIERLO, M. C. L. M. 1995 Laboratory measurements of the direction of sediment transport on transverse alluvial-bed slopes. *J. Hydr. Res.* **33**, 495–517.

TROWBRIDGE, J. H. 1995 A mechanism for the formation and maintenance of shore-oblique sand ridges on storm-dominated shelves. *J. Geophys. Res.* **100**, 16071–16086.

VAN RIJN, L. C. 1984 Sediment transport, part II: suspended load transport. *J. Hydr. Engng.* **110**, 1613–1641.

VAN RIJN, L. C. 1991 Sediment transport in combined waves and currents. *Proc. Euromech 262* (ed. R. Soulsby & R. Bettes). Balkema.

VAN RIJN, L. C., VAN ROSSUM, H. & TERNES, P. 1990 Field verification of 2-D and 3-D suspended-sediment models. *J. Hydr. Res.* **166**, 1270–1288.

VITTORI, G. 1989 Nonlinear viscuos oscillatory flow over a small amplitude wavy wall. *J. Hydraul. Res.* **27**, 267–280.

VITTORI, G., DE SWART, H. E. & BLONDEAUX, P. 1999 Crescentic bedforms in the nearshore region. *J. Fluid Mech.* **381**, 271–303.